



Synthesis of hierarchical bismuth-rich $\text{Bi}_4\text{O}_5\text{Br}_{x}\text{I}_{2-x}$ solid solutions for enhanced photocatalytic activities of CO_2 conversion and Cr(VI) reduction under visible light



Yang Bai^a, Liqun Ye^{a,b,*}, Ting Chen^a, Pingquan Wang^a, Li Wang^b, Xian Shi^a, Po Keung Wong^c

^a State Key Laboratory of Oil and Gas Reservoir Geology and Exploitation, School of Oil & Natural Gas Engineering, Southwest Petroleum University, Chengdu 610500, China

^b Key Laboratory of Ecological Security for Water Source Region of Mid-Line Project of South-to-North Water Diversion of Henan Province, College of Chemistry and Pharmaceutical Engineering, Nanyang Normal University, Nanyang 473061, China

^c School of Life Sciences, The Chinese University of Hong Kong, Shatin, NT, Hong Kong Special Administrative Region, China

ARTICLE INFO

Article history:

Received 1 August 2016

Received in revised form 15 October 2016

Accepted 24 October 2016

Available online 25 October 2016

Keywords:

$\text{Bi}_4\text{O}_5\text{Br}_{x}\text{I}_{2-x}$

Solid solution

Photocatalysis

CO_2 conversion

Cr(VI) removal

ABSTRACT

Bismuth oxyhalides (BiOX , $X = \text{Br}, \text{I}$) photocatalysts are rarely applied for photocatalytic reduction reaction with the photo-induced electron, as this is impeded by their low conduction band. As a widely used approach for enhancing the photocatalytic reduction activity, bismuth-rich strategy results the bismuth content of BiOX photocatalysts increasing. In this paper, a solid solutions of bismuth-rich $\text{Bi}_4\text{O}_5\text{Br}_{x}\text{I}_{2-x}$ were prepared applying the molecular precursor method. $\text{Bi}_4\text{O}_5\text{Br}_{x}\text{I}_{2-x}$ were characterized by X-ray diffraction (XRD), field emission scanning electron microscopy (FESEM), transmission electron microscopy (TEM), element mapping, Brunauer–Emmett–Teller surface analysis (BET), UV-vis diffuse reflectance spectroscopy (DRS), and X-ray photoelectron spectroscopy (XPS). The obtained photocatalytic data showed that $\text{Bi}_4\text{O}_5\text{Br}_{x}\text{I}_{2-x}$ solid solutions had higher photocatalytic activities than $\text{Bi}_4\text{O}_5\text{Br}_2$ and $\text{Bi}_4\text{O}_5\text{I}_2$. At an optimal ratio of $x = 1$, the $\text{Bi}_4\text{O}_5\text{BrI}$ photocatalyst showed the highest photocatalytic reduction activity for CO_2 conversion ($22.85 \mu\text{mol h}^{-1} \text{g}^{-1}$ CO generation, AQE was 0.372 at 400 nm) and Cr(VI) removal (88%). CO_2 adsorption data and CO_2 temperature programmed desorption (CO_2 -TPD) revealed that $\text{Bi}_4\text{O}_5\text{BrI}$ exhibited the highest chemical adsorption ability of CO_2 molecules. Photocurrent and electrochemical impedance (EIS) spectroscopy demonstrated the enhanced photo-induced carrier separation efficiency of $\text{Bi}_4\text{O}_5\text{BrI}$. These mechanistic studies suggest that $\text{Bi}_4\text{O}_5\text{Br}_{x}\text{I}_{2-x}$ solid solutions are excellent photocatalysts for solar fuel generation and environmental remediation.

© 2016 Elsevier B.V. All rights reserved.

1. Introduction

Energy and environmental resources are the most critical factors for human livelihood. Therefore, worldwide research focuses more and more on new technologies for developing new means of energy generation and environmental remediation. Recently, photocatalysis technology displayed great prospects for environmental remediation and solar fuel generation [1–5]. Photocatalysis technology uses semiconductor nanomaterials to decompose toxic pollutants, convert carbon dioxide (CO_2), and split water under solar light irradiation. For example, oxide-based (TiO_2 [6], ZnO [7],

SnO_2 [8]), sulfide-based (CdS [9], ZnS [10], SnS [11]), silver-based (AgX ($X = \text{Cl}, \text{Br}, \text{I}$) [12,13], Ag_3PO_4 [14], Ag_2CrO_4 [15]), and bismuth-based semiconductors (Bi_2MoO_6 [16], BiVO_4 [17], BiOX ($X = \text{Cl}, \text{Br}, \text{I}$) [18,19], $\text{Bi}_2\text{O}_2\text{CO}_3$ [20]) were used for photocatalysis. However, most oxides cannot absorb visible light [21,22]; sulfide- and silver-based semiconductors are unstable due to the leak of ion under light irradiation [23,24]; and bismuth-based semiconductors were rarely used for solar fuel generation due to their low photocatalytic reduction activity [25–27]. Among the above three types of photocatalysts, bismuth-based semiconductors of the type BiOX were suggested to be most promising due their unique layered structure [25–27], and more and more few-layer BiOX nanosheets are applied for photocatalytic reduction in solar fuel generation [28–30].

In order to enhance the photocatalytic reduction activity of BiOX semiconductors more effectively, the bismuth content of BiOX was increased. This bismuth-rich strategy exploits that the

* Corresponding author at: Southwest Petroleum University, Nanyang Normal University, China.

E-mail address: yeliquny@163.com (L. Ye).

conduction band (CB) potential can be altered by changing the bismuth content, as the CB of BiOX is mainly determined by the Bi 6p state [31–33]. Depending on the respective bismuth content, different bismuth-rich BiOX photocatalysts may display different photocatalytic reduction activities. For example, $\text{Bi}_{24}\text{O}_{31}\text{Br}_{10}$ can photoreduce Cr(VI) [34], $\text{Bi}_3\text{O}_4\text{Br}$, $\text{Bi}_5\text{O}_7\text{X}$ ($\text{X}=\text{Br}$ and I), and $\text{Bi}_{24}\text{O}_{31}\text{Cl}_{10}$ can effectively activate molecular oxygen [35–38], and $\text{Bi}_3\text{O}_4\text{Cl}$ and $\text{Bi}_{12}\text{O}_{17}\text{Cl}_2$ exhibit efficient photocatalytic reduction activities for H_2 generation under visible light [39,40]. Recently, our group synthesized $\text{Bi}_4\text{O}_5\text{X}_2$ ($\text{X}=\text{Br}$ and I) photocatalysts applying the molecular precursor method [41–43]. These photocatalysts showed high photocatalytic reduction activities for CO_2 conversion. Furthermore, we improved the activity of bismuth-rich BiOX photocatalysts ($\text{Bi}_x\text{O}_y\text{X}_z$) by performing coupling, using a co-catalyst and applying doping [43–46]. However, no solid solution of bismuth-rich BiOX has been reported so far. At present, the different bismuth-rich $\text{Bi}_x\text{O}_y\text{X}_z$ with same atom ratio and different halogen are obtained by the hydrothermal process at different pH values [47–49]. However, the non-uniform synthesis conditions of this approach cause difficulties in the synthesis of solid solutions of bismuth-rich BiOX.

In this paper, solid solutions of bismuth-rich $\text{Bi}_4\text{O}_5\text{Br}_x\text{I}_{2-x}$ were prepared via the molecular precursor method based on our previous work, and their enhanced photocatalytic mechanism was discussed in detail [42,43]. To the best of our knowledge, no solid solution of $\text{Bi}_4\text{O}_5\text{Br}_x\text{I}_{2-x}$ photocatalysts has been reported to date. At an optimal ratio of $x=1$, $\text{Bi}_4\text{O}_5\text{BrI}$ showed the highest photocatalytic reduction activity for CO_2 conversion ($22.85 \mu\text{mol h}^{-1} \text{g}^{-1}$ CO generation) and Cr(VI) removal (88%).

2. Experimental section

2.1. Materials

$\text{Bi}(\text{NO}_3)_3 \cdot 5\text{H}_2\text{O}$, KBr, KI, glycerol, and ethanol were purchased from Sinopharm Chemical Reagent Co., Ltd. (Shanghai, China). These reagents were of analytical grade and were used without further purification.

2.2. Synthesis

2.2.1. Complex precursor

Each of the reagents KX ($\text{X}=\text{Br}$ or/and I ; 2 mmol) and $\text{Bi}(\text{NO}_3)_3 \cdot 5\text{H}_2\text{O}$ (2 mmol) was dissolved in 20 mL glycerol. Then, the KX solution was added dropwise to the $\text{Bi}(\text{NO}_3)_3 \cdot 5\text{H}_2\text{O}$ solution while stirring continuously. The resulting suspension was transferred into Teflon-lined stainless steel autoclaves (50 mL) and kept at 160°C for 16 h. After the reaction was completed, the formed complex precursor precipitate was obtained by centrifugation and

$$\begin{aligned} \text{AQE } (\%) &= \frac{\text{N}_{\text{Solar fuels}}}{\text{N}_p} = \frac{2 \times \text{number of CO molecules}}{\text{the number of incident photons}} + \frac{8 \times \text{number of CH}_4 \text{ molecules}}{\text{the number of incident photons}} \times 100\% \\ &= \frac{2 \times N_a \times (M_{\text{CO}} + M_{\text{CH}_4})}{Pst\lambda} \end{aligned}$$

then washed with ethanol. Finally, the obtained complex precursor was dried at 80°C under air atmosphere.

2.3. $\text{Bi}_4\text{O}_5\text{Br}_x\text{I}_{2-x}$

$\text{Bi}_4\text{O}_5\text{Br}_x\text{I}_{2-x}$ compounds were synthesized by a simple hydrolytic process from an aqueous solution of their complex precursor molecules (0.3 g in 100 mL deionized water). The obtained $\text{Bi}_4\text{O}_5\text{Br}_x\text{I}_{2-x}$ compounds were washed successively with deionized water and finally dried at 80°C .

2.4. Characterization

X-Ray diffraction patterns (XRD) of the samples were recorded at room temperature with a Bruker D8 advance X-ray diffractometer using $\text{Cu K}\alpha$ radiation and a 2θ scan rate of 6 min^{-1} . Diffraction patterns were taken over an angular range of $2\theta=5\text{--}70^\circ$. A Sigma Zeiss field-emission scanning electron microscope (FESEM) was used to take FESEM images, and a JEOL JEM-2100F (RH) field-emission electron microscope was used to take transmission electron microscopy (TEM) and high-resolution transmission electron microscopy (HRTEM) images. X-ray photoelectron spectroscopy (XPS) measurements were carried out with a Thermo Scientific ESCALAB 250XI X-ray photoelectron spectrometer (Al $\text{K}\alpha$, 150 W, C1s 284.8 eV). UV-vis diffuse reflectance spectra (DRS) were obtained by UV-vis spectroscopy (Perkin Elmer, Lambda 650s, BaSO_4 as a reference). A Quantachrome Autosorb-IQ automated gas sorption system, operated at 77 K, was used to measure the Brunauer–Emmett–Teller (BET) surface areas and CO_2 adsorption properties. CO_2 temperature programmed desorption (CO_2 -TPD) was carried out on the instrument AutoChem II 2920 (Micrometrics). The CO_2 -TPD curves were obtained by gradually increasing the temperature to 500°C with a ramping rate of 1°C min^{-1} .

2.5. Photocatalytic CO_2 conversion

Photocatalytic CO_2 conversion was carried out in an off-line system. The used reactor. In the first step, 50 mg photocatalyst were uniformly dispersed on a glass sheet (about 25 cm^2 surface area). A mixture of $\text{CO}_2/\text{H}_2\text{O}$ vapor was produced by passing compressed high purity CO_2 gas (99.99%) through a water vaporizer. This $\text{CO}_2/\text{H}_2\text{O}$ vapor served as reaction gas and was introduced into the reaction system for several times to remove air. The reactor was purged for 15 min with $\text{CO}_2/\text{H}_2\text{O}$ vapor and subsequently irradiated with a 300 W high-pressure Xenon lamp (PLS-SXE300C, Beijing Perfectlight Technology Co., Ltd., Beijing, China.) equipped with a 400 nm filter. The photoreaction temperature was maintained at 15°C with a DC-0506 low-temperature thermostat bath (Shanghai Sunny Hengping Scientific Instrument Co., Ltd., Shanghai, China). 1 mL of gas was taken from the reaction cell at each time interval for qualitative analysis using an Agilent 7890 gas chromatograph equipped with a flame ionization detector (FID, Porapak N 80/100 columns) and a thermal conductivity detector (TCD, Molecular Sieve 13 \times 60/80 columns). The production yield was quantified using a calibration curve. The outlet gases were determined to be mainly CO, CH_4 , and small quantities of O_2 and H_2 .

400 nm monochromatic light (400 nm band-pass filter, the illumination intensity of the light at the sample surface was 1.23 mW/cm^2) was used to test the apparent quantum efficiency (AQE) by the following equation.

Where, $N_a = 6.02 \times 10^{23} \text{ mol}^{-1}$, $P = 1.23 \text{ mW/cm}^2$, $S = 25 \text{ cm}^2$, $t = 3600 \text{ s}$, $\lambda = 400 \times 10^{-9} \text{ m}$, $h = 6.626 \times 10^{-34} \text{ Js}$, and $c = 3 \times 10^8 \text{ m s}^{-1}$.

2.6. Photocatalytic Cr(VI) removal

$\text{Bi}_4\text{O}_5\text{Br}_x\text{I}_{2-x}$ powders (20 mg) were added to the prepared Cr(VI) solution (50 mL, $60 \text{ mg L}^{-1} \text{ K}_2\text{Cr}_2\text{O}_7$) while stirring (about 30 min) to attain adsorption equilibrium. A 300 W high-pressure xenon lamp equipped with a 400 nm filter (PLS-SXE300C, Beijing Perfect

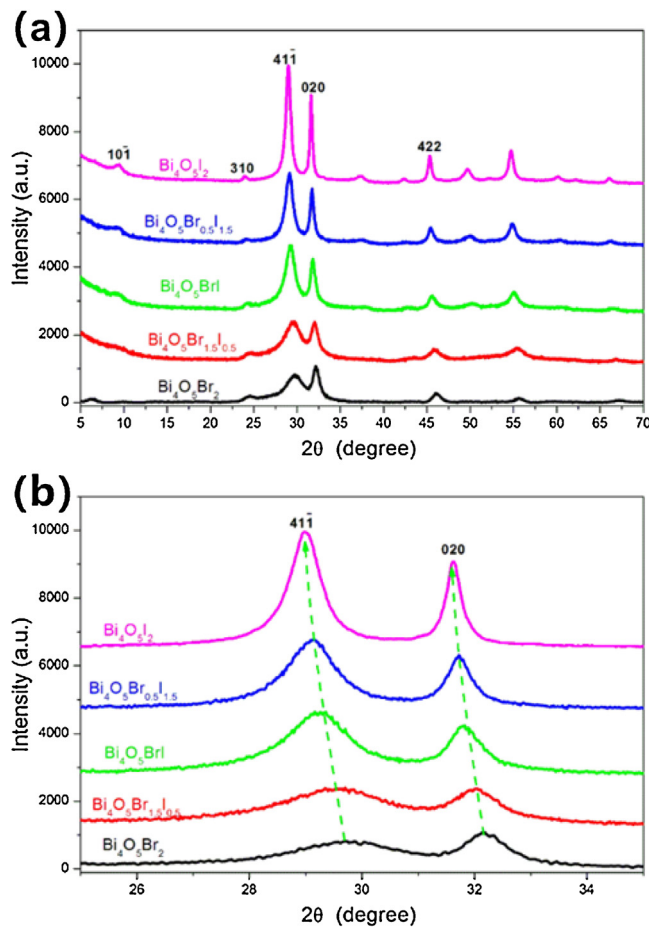


Fig. 1. XRD patterns of $\text{Bi}_4\text{O}_5\text{Br}_{x}\text{I}_{2-x}$ ($x=0, 0.5, 1, 1.5$, and 2): (a) 5° – 70° and (b) 25° – 35° .

light Technology Co., Ltd., Beijing, China) was used as light source. The suspensions were sampled (3 mL) at each given time interval and the samples were centrifuged to remove the powders. The concentration of $\text{K}_2\text{Cr}_2\text{O}_7$ was measured during the adsorption with a Lambda 650 s spectrophotometer.

2.7. Photoelectrochemical measurements

Mott–Schottky plots, transient photocurrent responses, and electrochemical impedance spectra (EIS) of the samples were recorded in a three-electrode quartz cell containing Na_2SO_4 (0.1 M) electrolyte solution and using a CHI660D electrochemical working station (CHI Instruments, Shanghai, China). Ag/AgCl and Pt were used as reference and counter electrodes, respectively. 15 μL of Nafion@117 solution (5 wt%) and 5 mg of samples were dispersed in a 1 mL water/isopropanol mixed solvent (3:1 v/v) by sonication to form a homogeneous colloid. And then, 0.1 mL colloid was deposited onto the fluorine doped tin oxide (FTO) glass as the working electrode.

3. Results and discussion

Fig. 1 shows the XRD patterns of the as-prepared semiconductors $\text{Bi}_4\text{O}_5\text{Br}_2$, $\text{Bi}_4\text{O}_5\text{Br}_{1.5}\text{I}_{0.5}$, $\text{Bi}_4\text{O}_5\text{BrI}$, $\text{Bi}_4\text{O}_5\text{Br}_{0.5}\text{I}_{1.5}$, and $\text{Bi}_4\text{O}_5\text{I}_2$. All these compounds show similar monoclinic structures. For $\text{Bi}_4\text{O}_5\text{Br}_2$, the diffraction peaks were in agreement with the standard XRD pattern of PDF: 00-037-0699 (space group: P21, unit cell parameters: $a = 1.452 \text{ nm}$, $b = 0.5625 \text{ nm}$, and $c = 1.083 \text{ nm}$, $\alpha = \gamma = 90.0^\circ$, $\beta = 97.6^\circ$) and also in accordance with previous work

[43]. For $\text{Bi}_4\text{O}_5\text{I}_2$, the diffraction peaks were in agreement with our results (space group: P21, unit cell parameters: $a = 1.494 \text{ nm}$, $b = 0.5698 \text{ nm}$, and $c = 1.126 \text{ nm}$, $\alpha = \gamma = 90.0^\circ$, $\beta = 99.8^\circ$) [41,42]. The enlarged part of the XRD patterns (Fig. 1b) shows that the diffraction peaks significantly shift toward lower angles along with an increasing I^- content of the semiconductor, owing to the smaller radius of Br^- with respect to I^- . This indicates that $\text{Bi}_4\text{O}_5\text{Br}_{1.5}\text{I}_{0.5}$, $\text{Bi}_4\text{O}_5\text{BrI}$, and $\text{Bi}_4\text{O}_5\text{Br}_{0.5}\text{I}_{1.5}$ are solid solutions rather than compounds intermediary between $\text{Bi}_4\text{O}_5\text{Br}_2$ and $\text{Bi}_4\text{O}_5\text{I}_2$. On the other hand, Fig. 1b shows that the diffraction peaks' widths at half height increase from $x = 0$ to 2, which is correlated to a decrease in the crystal size from $x = 0$ to 2. A possibly related decrease in the surface area from $x = 0$ to 2 will be checked by Brunauer–Emmett–Teller (BET) analysis.

The composition and chemical status of the samples were analyzed by X-ray photoelectron spectroscopy (XPS), as shown in Fig. 2a. The relevant XPS peak position is calibrated against the C1s signal of contaminant carbon at a binding energy of 284.6 eV. The survey spectrum showed that only Bi, O, Br, and/or I were detected. This confirms the high purity of the $\text{Bi}_4\text{O}_5\text{Br}_2$, $\text{Bi}_4\text{O}_5\text{I}_2$, and $\text{Bi}_4\text{O}_5\text{BrI}$ samples. The binding energies of the Bi 4f 7/2 and Bi 4f 5/2 peaks of $\text{Bi}_4\text{O}_5\text{Br}_2$, $\text{Bi}_4\text{O}_5\text{I}_2$, and $\text{Bi}_4\text{O}_5\text{BrI}$ (inset Table in Fig. 2b) suggest that these three samples contain Bi^{3+} . The band energies of 630.81 eV and 619.34 eV attributed to I 3d 5/2 and I 3d 3/2 (Fig. 2c) and are associated with I^- in $\text{Bi}_4\text{O}_5\text{BrI}$ and $\text{Bi}_4\text{O}_5\text{I}_2$, respectively. The binding energies of Br 3d 5/2 and Br 3d 3/2 of $\text{Bi}_4\text{O}_5\text{BrI}$ and $\text{Bi}_4\text{O}_5\text{Br}_2$, respectively, (inset Table in Fig. 2d) indicate the presence of Br^- in $\text{Bi}_4\text{O}_5\text{BrI}$ and $\text{Bi}_4\text{O}_5\text{Br}_2$. The atomic ratios (peak areas) of Bi:Br:I were 4:2:0, 4:0:2, and 4:1:1 for $\text{Bi}_4\text{O}_5\text{Br}_2$, $\text{Bi}_4\text{O}_5\text{I}_2$, and $\text{Bi}_4\text{O}_5\text{BrI}$, respectively. Those ratios were in agreement with their theoretical values.

Fig. 3 displays the morphology and element analysis of $\text{Bi}_4\text{O}_5\text{BrI}$. It was found that $\text{Bi}_4\text{O}_5\text{BrI}$ solid solution exhibits a structure of hierarchical microspheres with diameters of about 2–5 μm (Fig. 3a and c). The microspheres are assembled in ultrathin $\text{Bi}_4\text{O}_5\text{BrI}$ nanosheets (Fig. 3b and d), which contain three layers and have a total thickness of 3 nm. The HRTEM image also shows clear lattice spacing of 0.942 and 0.283 nm. In our previous work [50], the crystalline interplanar spacing of 0.969 and 0.285 nm were indexed to the {101} and {020} facets of $\text{Bi}_4\text{O}_5\text{I}_2$, and the crystalline interplanar spacings of 0.918 and 0.281 nm were indexed to the {101} and {020} facets of $\text{Bi}_4\text{O}_5\text{Br}_2$. Comparison of these values shows that the crystalline interplanar spacing of $\text{Bi}_4\text{O}_5\text{BrI}$ are between those of $\text{Bi}_4\text{O}_5\text{Br}_2$ and $\text{Bi}_4\text{O}_5\text{I}_2$. Therefore, the $\text{Bi}_4\text{O}_5\text{BrI}$ crystalline interplanar spacing of 0.942 and 0.283 nm were also indexed to the {101} and {020} facets of $\text{Bi}_4\text{O}_5\text{BrI}$, respectively. Scanning transmission electron microscopy (STEM) image (Fig. 3e) and the corresponding element mapping of $\text{Bi}_4\text{O}_5\text{BrI}$ show clearly and uniformly distributed Bi, Br, and I elements.

N_2 adsorption–desorption isotherms and Barrett–Joyner–Halenda (BJH) pore size distribution curves of $\text{Bi}_4\text{O}_5\text{Br}_2$, $\text{Bi}_4\text{O}_5\text{I}_2$, and $\text{Bi}_4\text{O}_5\text{BrI}$ are shown in Fig. 4. Specific surface areas calculated from the linear parts of the multipoint plots of $\text{Bi}_4\text{O}_5\text{Br}_2$, $\text{Bi}_4\text{O}_5\text{BrI}$, and $\text{Bi}_4\text{O}_5\text{I}_2$ were 99.3, 79.2, and $49.9 \text{ m}^2 \text{ g}^{-1}$, respectively, which are in agreement with the XRD analysis. The hysteresis loops were identified as type H3 loops. This indicates that the pores of $\text{Bi}_4\text{O}_5\text{Br}_2$, $\text{Bi}_4\text{O}_5\text{BrI}$, and $\text{Bi}_4\text{O}_5\text{I}_2$ are formed by non-rigid aggregates of plate-like particles [51], which has been confirmed by SEM and TEM images. The pore size distribution shows the existence of two different pore sizes. The first pore size was 3.7 nm for all above three samples. The second size was about 6 nm for $\text{Bi}_4\text{O}_5\text{Br}_2$ and $\text{Bi}_4\text{O}_5\text{BrI}$ (insertion of Fig. 4), which indicates that $\text{Bi}_4\text{O}_5\text{Br}_{x}\text{I}_{2-x}$ solid solutions maintain their large surface areas and mesoporous structures.

In past two years, the CO_2 conversion in solar fuels over BiOCl , BiOBr , BiOI , $\text{Bi}_5\text{O}_7\text{I}$, $\text{Bi}_4\text{O}_5\text{Br}_2$, and $\text{Bi}_4\text{O}_5\text{I}_2$ was studied, as shown in

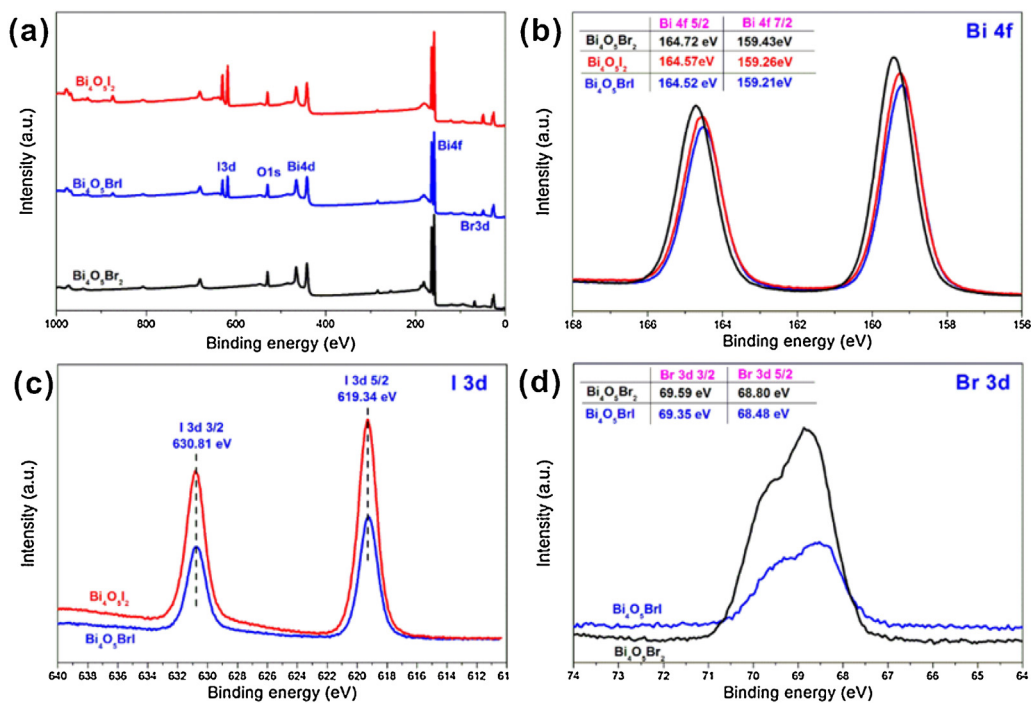


Fig. 2. XPS spectra of Bi₄O₅Br₂, Bi₄O₅BrI, and Bi₄O₅I₂: (a) survey, (b) Bi 4f, (c) I 3d, and (d) Br 3d.

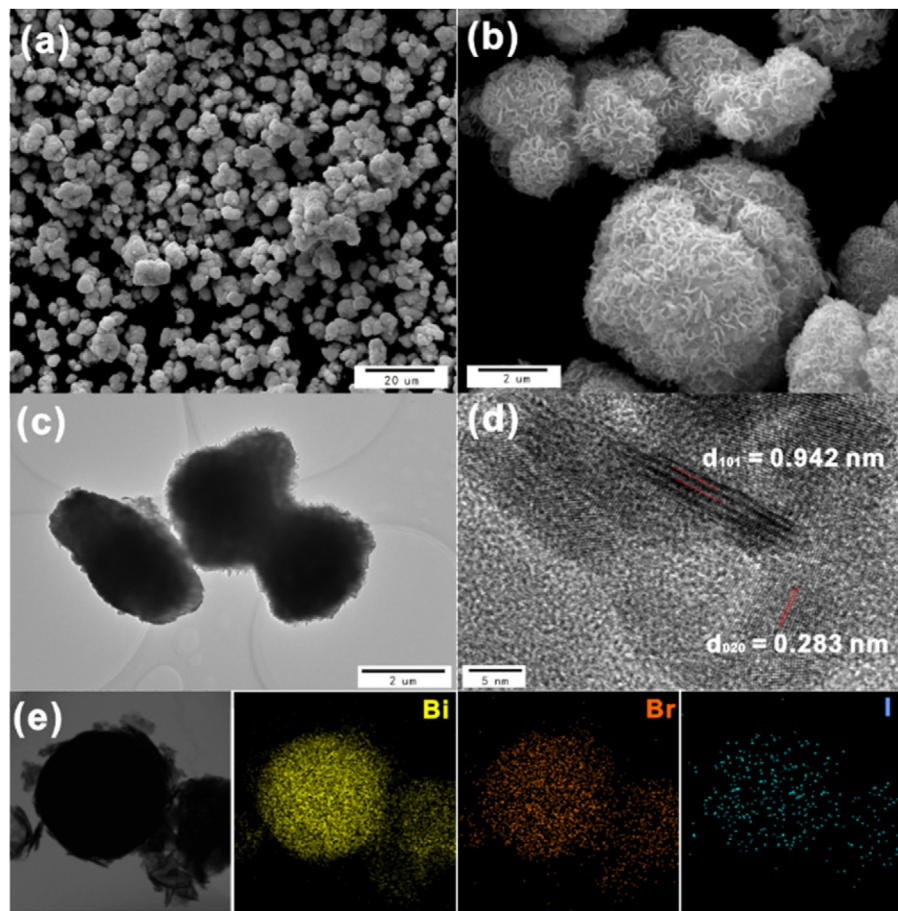


Fig. 3. (a) and (b) FESEM images, (c) TEM image, (d) HRTEM image, and (e) STEM images and the corresponding element mapping of Bi₄O₅BrI.

Table 1Comparison of TiO_2 , $\text{g-C}_3\text{N}_4$ and BiOX -based photocatalysts for CO_2 conversion.

Photocatalysts	Light source	$\text{CO} (\mu\text{mol h}^{-1} \text{g}^{-1})$	$\text{CH}_4 (\mu\text{mol h}^{-1} \text{g}^{-1})$	Refs.
TiO_2	300 W Xe lamp	NO	1.35	[52]
$\text{g-C}_3\text{N}_4$	300 W Xe lamp	1.97	1.94	[53]
BiOCl	500 W Xe lamp	1.01	0.15	[41]
BiOBr	300 W Xe lamp $\lambda > 400 \text{ nm}$	1.68	0.16	[43]
BiOI	300 W Xe lamp $\lambda > 420 \text{ nm}$	0.51	0.18	[29]
$\text{Bi}_5\text{O}_7\text{I}$	300 W Xe lamp $\lambda > 400 \text{ nm}$	1.73	0.18	[42]
$\text{Bi}_4\text{O}_5\text{Br}_2$	300 W Xe lamp $\lambda > 400 \text{ nm}$	2.71	1.65	This work
$\text{Bi}_4\text{O}_5\text{I}_2$	300 W Xe lamp $\lambda > 400 \text{ nm}$	15.87	0.18	
$\text{Bi}_4\text{O}_5\text{BrI}$	300 W Xe lamp $\lambda > 400 \text{ nm}$	22.85	2.13	

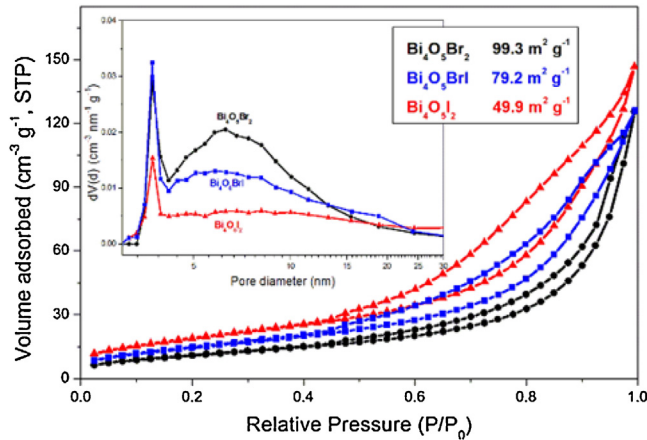
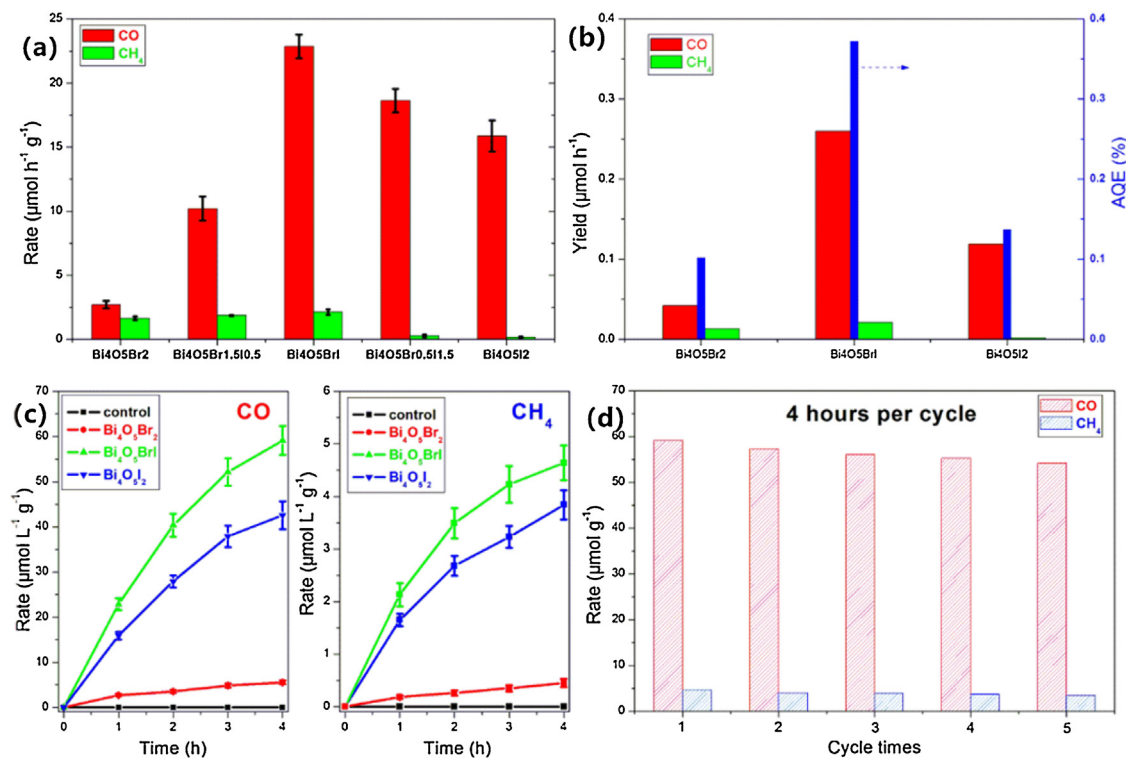
**Fig. 4.** N_2 adsorption–desorption isotherms and BJH pore size distribution curves (insertion) of $\text{Bi}_4\text{O}_5\text{Br}_2$, $\text{Bi}_4\text{O}_5\text{I}_2$, and $\text{Bi}_4\text{O}_5\text{BrI}$.

Table 1 [29,41–43]. We found that $\text{Bi}_4\text{O}_5\text{Br}_2$ and $\text{Bi}_4\text{O}_5\text{I}_2$ display better activities for photocatalytic CO_2 conversion with visible light radiation. In this work, we expected to find an enhanced activity for $\text{Bi}_4\text{O}_5\text{Br}_{x}\text{I}_{2-x}$ solid solutions. Fig. 5 shows the photocatalytic rates of products of CO_2 conversion over $\text{Bi}_4\text{O}_5\text{Br}_{x}\text{I}_{2-x}$ ($x=0, 0.5, 1, 1.5$, and 2) solid solutions under visible light irradiation for 1 h. It exhibits that CO and CH_4 were generated during the photocatalytic CO_2 conversion, and CO was the main product. The best photocatalyst was $\text{Bi}_4\text{O}_5\text{BrI}$ with a photocatalytic rate of $22.85 \mu\text{mol h}^{-1} \text{g}^{-1}$, which was about 8.4 times larger than that of pure $\text{Bi}_4\text{O}_5\text{Br}_2$ ($2.71 \mu\text{mol h}^{-1} \text{g}^{-1}$) and 1.4 times larger than that of pure $\text{Bi}_4\text{O}_5\text{I}_2$ ($15.87 \mu\text{mol h}^{-1} \text{g}^{-1}$). And at 400 nm monochromatic light irradiation, Fig. 5b showed the apparent quantum efficiency (AQE) of $\text{Bi}_4\text{O}_5\text{BrI}$ reached 0.372%. It was about 3.65 and 2.72 times of $\text{Bi}_4\text{O}_5\text{Br}_2$ (0.102%) and $\text{Bi}_4\text{O}_5\text{I}_2$ (0.137%), respectively. Fig. 5c and d display the photocatalytic yields of CO and CH_4 , respectively, under visible light irradiation for different times. They reveal that the total yields of CO and CH_4 increased with the irradiation time, whereas the yields decreased due to the possible pressure change. The cyclic experiment (Fig. 5d) revealed that the photocatalytic activity of $\text{Bi}_4\text{O}_5\text{BrI}$ decreased about 8% within five cycles (4 h)

**Fig. 5.** (a) Rates of products for $\text{Bi}_4\text{O}_5\text{Br}_{x}\text{I}_{2-x}$ ($x=0, 0.5, 1, 1.5$, and 2) under visible light irradiation for 1 h; (b) apparent quantum efficiency and gas yield of $\text{Bi}_4\text{O}_5\text{Br}_2$, $\text{Bi}_4\text{O}_5\text{BrI}$, and $\text{Bi}_4\text{O}_5\text{I}_2$ under 400 nm monochromatic light irradiation, yields of (c) CO and CH_4 over $\text{Bi}_4\text{O}_5\text{Br}_2$, $\text{Bi}_4\text{O}_5\text{BrI}$, and $\text{Bi}_4\text{O}_5\text{I}_2$ under visible light irradiation for different times, and (d) cyclic experiment over $\text{Bi}_4\text{O}_5\text{BrI}$ under visible light irradiation for 4 h per circulation.

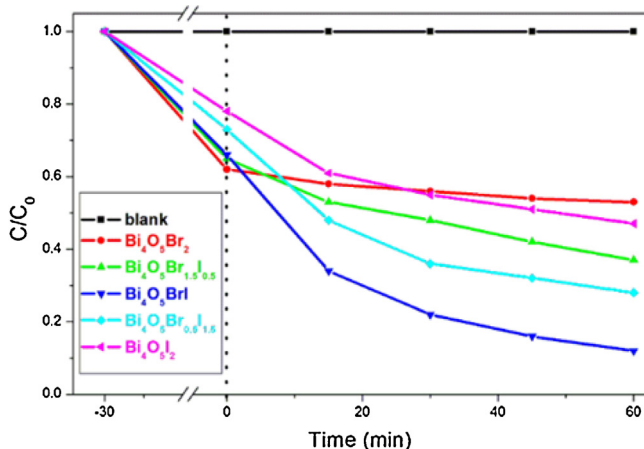


Fig. 6. Photocatalytic activities of $\text{Bi}_4\text{O}_5\text{Br}_{x}\text{I}_{2-x}$ ($x = 0, 0.5, 1, 1.5$, and 2) for Cr(VI) removal under visible light.

per cycle). However, the photocatalytic rate of the fifth cycle of $\text{Bi}_4\text{O}_5\text{BrI}$ ($54.2 \mu\text{mol g}^{-1}$) was still higher than that of $\text{Bi}_4\text{O}_5\text{I}_2$ ($42.5 \mu\text{mol g}^{-1}$) and $\text{Bi}_4\text{O}_5\text{Br}_2$ ($5.5 \mu\text{mol g}^{-1}$). On the other hand, the XRD patterns of $\text{Bi}_4\text{O}_5\text{BrI}$ before and after photocatalytic cycle tests also proved the stabilization of $\text{Bi}_4\text{O}_5\text{Br}_{x}\text{I}_{2-x}$ solid solutions.

Besides the photocatalytic CO_2 reduction in the gaseous phase, we evaluated the photocatalytic Cr(VI) reduction activity in the liquid phase (Fig. 6). Control experiments with absence of photocatalysts did not show any changes under visible light. The evaluation of the photocatalytic Cr(VI) reduction activity in the liquid phase revealed that after 30 min adsorption and 60 min visible light irradiation, the Cr(VI) removal ratios were 47, 63, 88, 72, and 53% for $\text{Bi}_4\text{O}_5\text{Br}_2$, $\text{Bi}_4\text{O}_5\text{Br}_{1.5}\text{I}_{0.5}$, $\text{Bi}_4\text{O}_5\text{BrI}$, $\text{Bi}_4\text{O}_5\text{Br}_{0.5}\text{I}_{1.5}$, and $\text{Bi}_4\text{O}_5\text{I}_2$, respectively. This indicates that $\text{Bi}_4\text{O}_5\text{Br}_{x}\text{I}_{2-x}$ solid solutions show higher photocatalytic reduction activities than $\text{Bi}_4\text{O}_5\text{Br}_2$ and $\text{Bi}_4\text{O}_5\text{I}_2$ for Cr(VI) removal with an optimal activity for $x = 1$. This implies that the solid solution strategy is a practical approach for enhancing the photocatalytic activity of bismuth-rich BiOX photocatalysts.

The photocatalytic CO_2 conversion is intensely affected by substrate adsorption properties. In order to compare the interaction between CO_2 molecules and $\text{Bi}_4\text{O}_5\text{Br}_{x}\text{I}_{2-x}$, we studied the CO_2 adsorption and CO_2 temperature programmed desorption (CO_2 -TPD) profiles of $\text{Bi}_4\text{O}_5\text{I}_2$, $\text{Bi}_4\text{O}_5\text{BrI}$, and $\text{Bi}_4\text{O}_5\text{I}_2$ (Fig. 7). As shown in Fig. 7a, $\text{Bi}_4\text{O}_5\text{BrI}$ absorbs a much larger number of CO_2 molecules, although $\text{Bi}_4\text{O}_5\text{BrI}$ has a smaller surface area than $\text{Bi}_4\text{O}_5\text{Br}_2$. This may be due to the different adsorption characteristics of N_2 and CO_2 on $\text{Bi}_4\text{O}_5\text{Br}_{x}\text{I}_{2-x}$ surfaces. N_2 adsorption–desorption isotherms reflect the physical adsorption to evaluate the surface area of the material. For non-carbon $\text{Bi}_4\text{O}_5\text{Br}_{x}\text{I}_{2-x}$ catalysts, CO_2 adsorption should reflect the chemical adsorption for an evaluation of the active site of the CO_2 reaction on the material [51]. CO_2 -TPD confirmed that CO_2 adsorbed chemically on the $\text{Bi}_4\text{O}_5\text{Br}_{x}\text{I}_{2-x}$ surface. As shown in Fig. 7b, only $\text{Bi}_4\text{O}_5\text{Br}_2$ released a few CO_2 molecules at a desorption temperature of less than 200°C . This temperature range is attributed to physical absorption and is in agreement with the BET data. When desorption temperature was larger than 200°C (chemical adsorption range), we found that $\text{Bi}_4\text{O}_5\text{BrI}$ released much more CO_2 than $\text{Bi}_4\text{O}_5\text{Br}_2$ and $\text{Bi}_4\text{O}_5\text{I}_2$. This indicates that the solid solution strategy was an effective method to enhance the chemical adsorption of CO_2 . However, the reason for this remains to be studied. It is important to stress that BET data (N_2 adsorption–desorption isotherm) cannot be used to arbitrarily evaluate substrate molecule adsorption abilities.

It has been proven that the CB position of photocatalysts determines the photocatalytic reduction activity of photo-induced

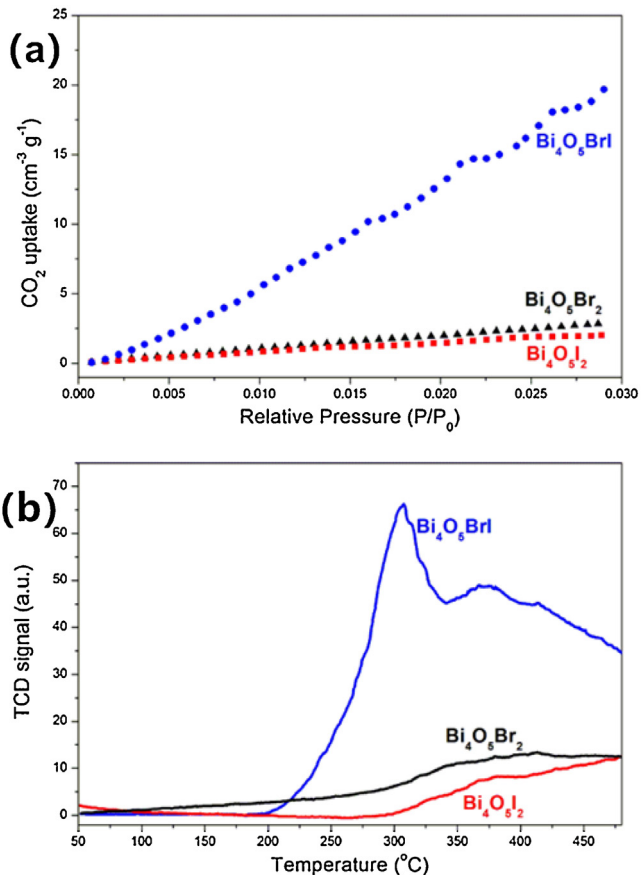


Fig. 7. (a) CO_2 adsorption and (b) CO_2 -TPD profiles of $\text{Bi}_4\text{O}_5\text{I}_2$, $\text{Bi}_4\text{O}_5\text{BrI}$, and $\text{Bi}_4\text{O}_5\text{I}_2$.

electrons. Higher CB positions induced higher photocatalytic reduction activities. In order to compare the CB positions of $\text{Bi}_4\text{O}_5\text{Br}_2$, $\text{Bi}_4\text{O}_5\text{BrI}$, and $\text{Bi}_4\text{O}_5\text{I}_2$, UV-vis diffuse reflectance spectra (DRS) and valence band XPS (VB XPS) spectra were recorded (Fig. 8). UV-vis diffuse absorption spectra (Fig. 8a) display that $\text{Bi}_4\text{O}_5\text{I}_2$, $\text{Bi}_4\text{O}_5\text{BrI}$, and $\text{Bi}_4\text{O}_5\text{I}_2$ absorb in the visible light. However, they displayed different absorption edges. The band-edge of optical absorption of $\text{Bi}_4\text{O}_5\text{Br}_2$, $\text{Bi}_4\text{O}_5\text{BrI}$, and $\text{Bi}_4\text{O}_5\text{I}_2$ were about 488, 531, and 569 nm, respectively. Based on the relationship $E_g = 1240/\lambda$ of band gap (E_g) and absorption edge (λ) [54,55], the band gap energies of $\text{Bi}_4\text{O}_5\text{Br}_2$, $\text{Bi}_4\text{O}_5\text{BrI}$, and $\text{Bi}_4\text{O}_5\text{I}_2$ were evaluated to be 2.45, 2.34, and 2.18 eV, respectively. The VB-XPS spectra displayed that the VB positions of $\text{Bi}_4\text{O}_5\text{Br}_2$, $\text{Bi}_4\text{O}_5\text{BrI}$, and $\text{Bi}_4\text{O}_5\text{I}_2$ were 1.48, 1.64, and 1.99 V (Fig. 8b), respectively. Based on the equation $E_g = E_{\text{VB}} - E_{\text{CB}}$, the CB positions of $\text{Bi}_4\text{O}_5\text{Br}_2$, $\text{Bi}_4\text{O}_5\text{BrI}$, and $\text{Bi}_4\text{O}_5\text{I}_2$ were calculated to be -0.55 and -0.70 V, respectively. Fig. 8c exhibits that the CB edges of $\text{Bi}_4\text{O}_5\text{BrI}$ and $\text{Bi}_4\text{O}_5\text{I}_2$ are higher than that of $\text{Bi}_4\text{O}_5\text{Br}_2$, which results in higher photocatalytic activities for CO_2 conversion.

It is well known that the photocatalytic activity is usually affected by the photo-induced carrier separation efficiency. For proving this point for our samples, electrochemical impedance and photocurrent response spectra of $\text{Bi}_4\text{O}_5\text{Br}_2$, $\text{Bi}_4\text{O}_5\text{BrI}$, and $\text{Bi}_4\text{O}_5\text{I}_2$ were compared, as shown in Fig. 9. The photocurrent for $\text{Bi}_4\text{O}_5\text{BrI}$ revealed to be much higher than those of $\text{Bi}_4\text{O}_5\text{Br}_2$ and $\text{Bi}_4\text{O}_5\text{I}_2$ upon light irradiation (Fig. 9a). On the other hand, the diameter of the semicircle arc of $\text{Bi}_4\text{O}_5\text{BrI}$ was smaller than those of $\text{Bi}_4\text{O}_5\text{Br}_2$ and $\text{Bi}_4\text{O}_5\text{I}_2$ (Fig. 9b), which indicates that $\text{Bi}_4\text{O}_5\text{Br}_{x}\text{I}_{2-x}$ solid solutions have lower electron-transfer resistance values. Therefore, the mobility and separation efficiencies of the photo-induced carriers was efficaciously improved by using the solid solution strategy for $\text{Bi}_4\text{O}_5\text{X}_2$ ($\text{X} = \text{Br}$ and I) photocatalysts.

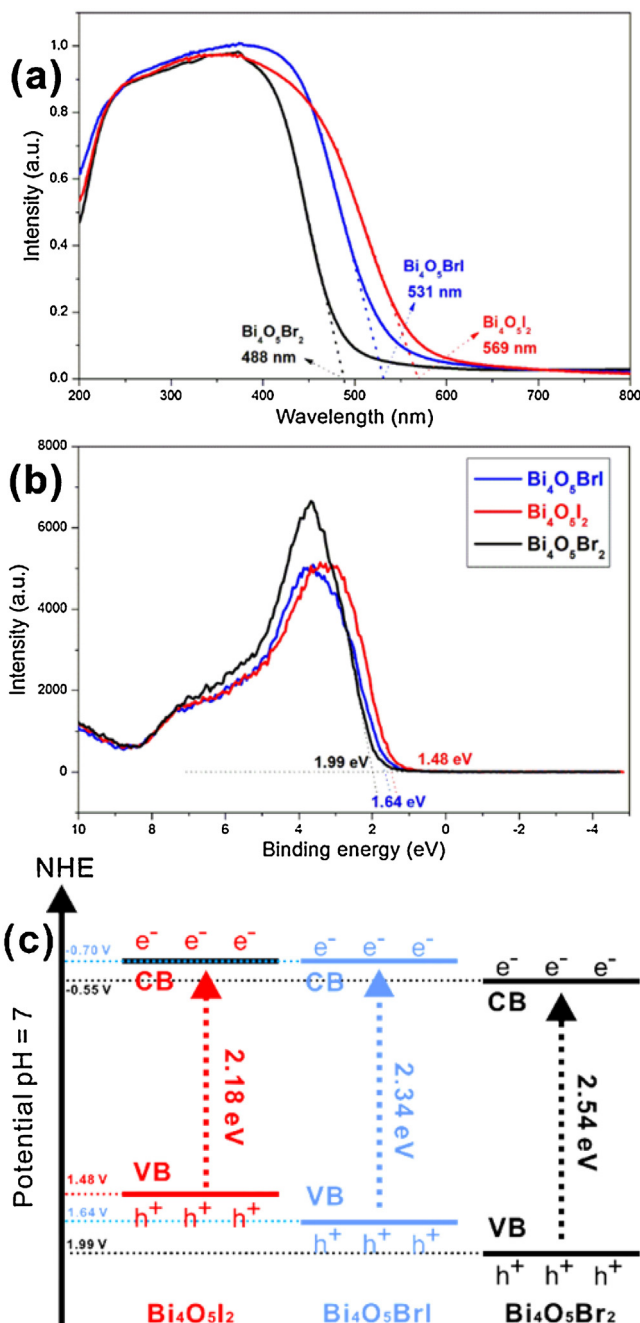


Fig. 8. (a) DRS and (b) valence band XPS spectra and (c) diagram of the band energies of $\text{Bi}_4\text{O}_5\text{Br}_2$, $\text{Bi}_4\text{O}_5\text{Brl}$, and $\text{Bi}_4\text{O}_5\text{I}_2$.

4. Conclusion

In this work, hierarchical bismuth-rich $\text{Bi}_4\text{O}_5\text{Br}_{x}\text{I}_{2-x}$ solid solutions were prepared and characterized by XRD, FESEM, TEM, BET, and XPS. The photocatalytic reduction data for CO_2 conversion and Cr(VI) removal showed that $\text{Bi}_4\text{O}_5\text{Br}_{x}\text{I}_{2-x}$ exhibit the highest photocatalytic reduction activity for an optimal ratio of $x=1$ with a CO production of $22.85 \mu\text{mol h}^{-1} \text{g}^{-1}$ and a Cr(VI) removal of 88% within 1 h. CO_2 adsorption data and CO_2 -TPD of $\text{Bi}_4\text{O}_5\text{Brl}$ revealed the highest ability for capturing CO_2 molecules among the studied samples. Band energy structure analysis showed a high CB position for the reduction over $\text{Bi}_4\text{O}_5\text{Br}_{x}\text{I}_{2-x}$ solid solutions. Photocurrent and EIS revealed that $\text{Bi}_4\text{O}_5\text{Br}_{x}\text{I}_{2-x}$ solid solutions exhibit higher photo-induced carrier separation efficiencies than $\text{Bi}_4\text{O}_5\text{Br}_2$

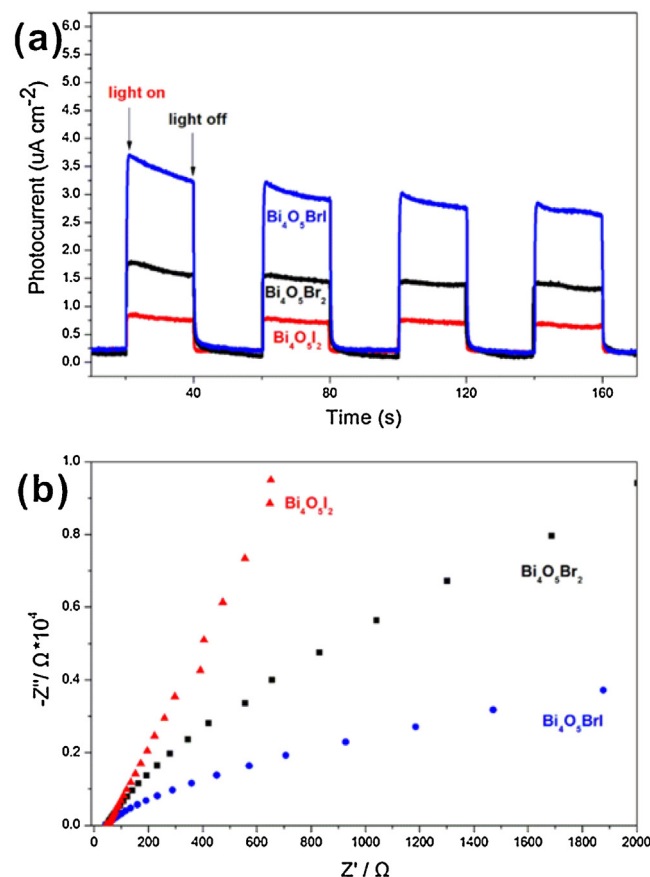


Fig. 9. (a) Electrochemical impedance and (b) photocurrent response spectra of $\text{Bi}_4\text{O}_5\text{Br}_2$, $\text{Bi}_4\text{O}_5\text{Brl}$, and $\text{Bi}_4\text{O}_5\text{I}_2$.

and $\text{Bi}_4\text{O}_5\text{I}_2$. Concluding, $\text{Bi}_4\text{O}_5\text{Br}_x\text{I}_{2-x}$ solid solutions display higher photocatalytic reduction activities than $\text{Bi}_4\text{O}_5\text{Br}_2$ and $\text{Bi}_4\text{O}_5\text{I}_2$. More importantly, we report here for the first time the synthesis of bismuth-rich $\text{Bi}_4\text{O}_5\text{X}_2$ solid solutions. This significantly enlarges the scope of applications of solid solutions of bismuth-based photocatalytic materials from BiOX solid solutions to bismuth-rich BiOX solid solutions.

Acknowledgments

This work was supported by Open Fund (PLN201615) of State Key Laboratory of Oil and Gas Reservoir Geology and Exploitation (Southwest Petroleum University), National Natural Science Foundation of China (No. 51502146, U1404506), Natural Science Foundation of Henan Department of Education (No. 14A150021), Scientific Research Starting Project of SWPU (No. 2015QHZ001), and Young Scholars Development Fund of SWPU (No. 201499010100).

Appendix A. Supplementary data

Supplementary data associated with this article can be found, in the online version, at <http://dx.doi.org/10.1016/j.apcatb.2016.10.066>.

References

- [1] M.R. Hoffmann, S.T. Martin, W. Choi, D.W. Bahnemann, Environmental applications of semiconductor photocatalysis, *Chem. Rev.* 95 (1) (1995) 69–96.

[2] K. Rajeshwar, N.R. de Tacconi, Solution combustion synthesis of oxide semiconductors for solar energy conversion and environmental remediation, *Chem. Soc. Rev.* 38 (2009) 1984–1998.

[3] X. Chen, S. Shen, L. Guo, S.S. Mao, Semiconductor-based photocatalytic hydrogen generation, *Chem. Rev.* 110 (2010) 6503–6570.

[4] A. Kubacka, M. Fernandez-Garcia, G. Colon, Advanced nanoarchitectures for solar photocatalytic applications, *Chem. Rev.* 112 (2012) 1555–1614.

[5] C. Dong, M. Xing, J. Zhang, Double-cocatalysts promote charge separation efficiency in CO_2 photoreduction: spatial location matters, *Mater. Horiz.* (2016), <http://dx.doi.org/10.1039/C6MH00210B>.

[6] C. Dong, M. Xing, J. Zhang, Economic hydrophobicity triggering of CO_2 photoreduction for selective CH_4 generation on noble-metal-free $\text{TiO}_2\text{-SiO}_2$, *J. Phys. Chem. Lett.* 7 (2016) 2962–2966.

[7] Z.R. Tian, J.A. Voigt, J. Liu, B. Mckenzie, M.J. Mcdermott, M.A. Rodriguez, H. Konishi, H. Xu, Complex and oriented ZnO nanostructures, *Nat. Mater.* 2 (2003) 821–826.

[8] S. Wu, H. Cao, S. Yin, X. Liu, X. Zhang, Amino acid-assisted hydrothermal synthesis and photocatalysis of SnO_2 nanocrystals, *J. Phys. Chem. C* 113 (41) (2009) 17893–17898.

[9] Q. Li, B. Guo, J. Yu, J. Ran, B. Zhang, H. Yan, J.R. Gong, Highly efficient visible-light-driven photocatalytic hydrogen production of CdS -cluster-decorated graphene nanosheets, *J. Am. Chem. Soc.* 133 (28) (2011) 10878–10884.

[10] J.S. Hu, LL. Ren, Y.G. Guo, H.P. Liang, A.M. Cao, L.J. Wan, C.L. Bai, Nanostructures mass production and high photocatalytic activity of ZnS nanoporous nanoparticles, *Angew. Chem.* 117 (2005) 1295–1299.

[11] Y.C. Zhang, J. Li, M. Zhang, D.D. Dionysiou, Size-tunable hydrothermal synthesis of SnS_2 nanocrystals with high performance in visible light-driven photocatalytic reduction of aqueous Cr(VI), *Environ. Sci. Technol.* 45 (21) (2011) 9324–9331.

[12] S. Liu, J. Yue, A. Gedanken, Synthesis of long silver nanowires from AgBr nanocrystals, *Adv. Mater.* 13 (2001) 656–658.

[13] C. An, S. Peng, Y. Sun, Facile synthesis of sunlight-driven $\text{AgCl}:\text{Ag}$ plasmonic nanophotocatalyst, *Adv. Mater.* 22 (2010) 2570–2574.

[14] Z. Yi, J. Ye, N. Kikugawa, T.K.S. Ouyang, H. Stuart-Williams, H. Yang, J. Cao, W. Luo, Z. Li, Y. Liu, R.L. Withers, An orthophosphate semiconductor with photooxidation properties under visible-light irradiation, *Nat. Mater.* 9 (2010) 559–564.

[15] Y. Liu, H. Yu, M. Cai, J. Sun, Microwave hydrothermal synthesis of Ag_2CrO_4 photocatalyst for fast degradation of PCP-Na under visible light irradiation, *Catal. Commun.* 26 (2012) 63–67.

[16] L. Zhang, T. Xu, X. Zhao, Y. Zhu, Controllable synthesis of Bi_2MoO_6 and effect of morphology and variation in local structure on photocatalytic activities, *Appl. Catal. B: Environ.* 98 (2010) 138–146.

[17] R. Li, F. Zhang, D. Wang, J. Yang, M. Li, J. Zhu, X. Zhou, H. Han, C. Li, Spatial separation of photogenerated electrons and holes among {010} and {110} crystal facets of BiVO_4 , *Nat. Commun.* 4 (1432) (7pp).

[18] Z. Zhang, F. Ai, L. Jia, Generalized one-pot synthesis, characterization, and photocatalytic activity of hierarchical BiOX ($X = \text{Cl}, \text{Br}, \text{I}$) nanoplate microspheres, *J. Phys. Chem. C* 112 (3) (2008) 747–753.

[19] J. Henle, P. Simon, A. Frenzel, S. Scholz, S. Kaskel, Nanosized BiOX ($X = \text{Cl}, \text{Br}, \text{I}$) particles synthesized in reverse microemulsions, *Chem. Mater.* 19 (3) (2007) 366–373.

[20] H. Huang, X.W. Li, J. Wang, F. Dong, P.K. Chu, T. Zhang, Y. Zhang, Anionic group self-doping as a promising strategy: band-gap engineering and multi-functional applications of high-performance CO_3^{2-} doped $\text{Bi}_2\text{O}_2\text{CO}_3$, *ACS Catal.* 5 (2015) 4094–4103.

[21] J. Xu, X. Zhou, Z. Gao, Y.Y. Song, P. Schmuki, Visible-light-triggered drug release from TiO_2 nanotube arrays: a controllable antibacterial platform, *Angew. Chem.* 128 (2016) 603–607.

[22] P. Zhang, T. Tachikawa, M. Fujitsuka, T. Majima, In situ fluorine doping of TiO_2 superstructures for efficient visible-light driven hydrogen generation, *ChemSusChem* 9 (2016) 617–623.

[23] C. An, J. Wang, W. Jiang, M. Zhang, X. Ming, S. Wang, Q. Zhang, Strongly visible-light responsive plasmonic shaped $\text{AgX}:\text{Ag}$ ($X = \text{Cl}, \text{Br}$) nanoparticles for reduction of CO_2 to methanol, *Nanoscale* 4 (2012) 5646–5650.

[24] M. Zhu, P. Chen, M. Liu, Graphene oxide enwrapped Ag/AgX ($X = \text{Br}, \text{Cl}$) nanocomposite as a highly efficient visible-light plasmonic photocatalyst, *ACS Nano* 5 (6) (2011) 4529–4536.

[25] H. Huang, Y. He, Z. Lin, L. Kang, Y. Zhang, Two novel Bi-based borate photocatalysts: crystal structure, electronic structure, photoelectrochemical properties, and photocatalytic activity under simulated solar light irradiation, *J. Phys. Chem. C* 117 (2013) 22986–22994.

[26] L. Ye, Y. Su, X. Jin, H. Xie, C. Zhang, Recent advances in BiOX ($X = \text{Cl}, \text{Br}$ and I) photocatalysts: synthesis, modification, facet effects and mechanisms, *Environ. Sci.: Nano* 1 (2014) 90–112.

[27] H. Huang, X. Han, X. Li, S. Wang, P.K. Chu, Y. Zhang, Multiple heterojunctions fabrication with tunable visible-light-active photocatalytic reactivity in the $\text{BiOBr}-\text{BiOI}$ full range composites based on microstructure modulation and band structures, *ACS Appl. Mater. Interfaces* 7 (2015) 482–492.

[28] M. Guan, C. Xiao, J. Zhang, S. Fan, R. An, Q. Cheng, J. Xie, M. Zhou, B. Ye, Y. Xie, Vacancy associates promoting solar-driven photocatalytic activity of ultrathin bismuth oxychloride nanosheets, *J. Am. Chem. Soc.* 135 (28) (2013) 10411–10417.

[29] L. Ye, H. Wang, X. Jin, Y. Su, D. Wang, H. Xie, X. Liu, X. Liu, Synthesis of olive-green few-layered BiOI for efficient photoreduction of CO_2 into solar fuels under visible/near-infrared light, *Sol. Energy Mater. Sol. Cells* 144 (2016) 732–739.

[30] L. Ye, X. Jin, Y. Leng, Y. Su, H. Xie, C. Liu, Synthesis of black ultrathin BiOCl nanosheets for efficient photocatalytic H_2 production under visible light irradiation, *J. Power Sources* 293 (2015) 409–415.

[31] Z. Xu, W. Hao, Q. Zhang, Z. Fu, H. Feng, Y. Du, S. Dou, Indirect-direct band transformation of few-layer BiOCl under biaxial strain, *J. Phys. Chem. C* 120 (16) (2016) 8589–8594.

[32] W.L. Huang, Q. Zhu, DFT calculations on the electronic structures of BiOX ($X = \text{F}, \text{Cl}, \text{Br}, \text{I}$) photocatalysts with and without semicore $\text{Bi}5d$ states, *J. Comput. Chem.* 30 (2009) 183–190.

[33] X. Zhang, B. Li, J. Wang, Y. Yuan, Q. Zhang, Z. Gao, L.M. Liu, L. Chen, The stabilities and electronic structures of single-layer bismuth oxyhalides for photocatalytic water splitting, *Phys. Chem. Chem. Phys.* 16 (2014) 25854–25861.

[34] J. Shang, W. Hao, X. Lv, T. Wang, X. Wang, Y. Du, S. Dou, T. Xie, D. Wang, J. Wang, Bismuth oxybromide with reasonable photocatalytic reduction activity under visible light, *ACS Catal.* 4 (3) (2014) 954–961.

[35] J. Wang, Y. Yu, L. Zhang, Highly efficient photocatalytic removal of sodium pentachlorophenate with $\text{Bi}_3\text{O}_4\text{Br}$ under visible light, *Appl. Catal. B: Environ.* 136–137 (2013) 112–121.

[36] X. Jin, L. Ye, H. Wang, Y. Su, H. Xie, Z. Zhong, H. Zhang, Bismuth rich strategy induced photocatalytic molecular oxygen activation properties of bismuth oxyhalogen: the case of $\text{Bi}_{24}\text{O}_{31}\text{Cl}_{10}$, *Appl. Catal. B: Environ.* 165 (2015) 668–675.

[37] Y. Su, C. Ding, Y. Dang, H. Wang, L. Ye, X. Jin, H. Xie, C. Liu, First hydrothermal synthesis of $\text{Bi}_5\text{O}_7\text{Br}$ and its photocatalytic properties for molecular oxygen activation and RhB degradation, *Appl. Surf. Sci.* 346 (2015) 311–316.

[38] Y. Su, H. Wang, L. Ye, X. Jin, H. Xie, C. He, K. Bao, Shape dependent photocatalytic activity of $\text{Bi}_5\text{O}_7\text{I}$ caused by facets synergistic and internal electric field effects, *RSC Adv.* 4 (2014) 65056–65064.

[39] J. Li, L. Cai, J. Shang, Y. Yu, L. Zhang, Giant enhancement of internal electric field boosting bulk charge separation for photocatalysis, *Adv. Mater.* 21 (2016) 4059–4064.

[40] H. Huang, K. Xiao, Y. He, T. Zhang, F. Dong, X. Du, Y. Zhang, In situ assembly of $\text{BiOI}@\text{Bi}_{12}\text{O}_{17}\text{Cl}_2$ p-n junction: charge induced unique front-lateral surfaces coupling heterostructure with high exposure of BiOI {001} active facets for robust and nonselective photocatalysis, *Appl. Catal. B: Environ.* 199 (2016) 75–86.

[41] L. Zhang, W. Wang, D. Jiang, E. Gao, S. Sun, Photoreduction of CO_2 on BiOCl nanoplates with the assistance of photoinduced oxygen vacancies, *Nano Res.* 8 (2015) 821–831.

[42] C. Ding, L. Ye, Q. Zhao, Z. Zhong, K. Liu, H. Xie, K. Bao, X. Zhang, Z. Huang, Synthesis of $\text{Bi}_5\text{O}_7\text{I}_2$ from molecular precursor and selective photoreduction of CO_2 into CO , *J. CO₂ Util.* 14 (2016) 135–142.

[43] L. Ye, X. Jin, C. He, C. Ding, H. Xie, K.H. Chu, P.K. Wong, Thickness-ultrathin and bismuth-rich strategies for BiOBr to enhance photoreduction of CO_2 into solar fuels, *Appl. Catal. B: Environ.* 187 (2016) 281–290.

[44] L. Zhang, W. Wang, S. Sun, Z. Zhang, J. Xu, J. Ren, Photocatalytic activity of Er^{3+} , Yb^{3+} doped $\text{Bi}_5\text{O}_7\text{I}$, *Catal. Commun.* 26 (2012) 88–92.

[45] Y. Huang, Y. He, M. Cui, Q. Nong, J. Yu, F. Wu, X. Meng, Synthesis of $\text{AgCl}/\text{Bi}_3\text{O}_4\text{Cl}$ composite and its photocatalytic activity in RhB degradation under visible light, *Catal. Commun.* 76 (2016) 19–22.

[46] Y. Peng, P.P. Yu, Q.G. Chen, H.Y. Zhou, A.W. Xu, Facile fabrication of $\text{Bi}_{12}\text{O}_{17}\text{Br}_2/\text{Bi}_{24}\text{O}_{31}\text{Br}_{10}$ type II heterostructures with high visible photocatalytic activity, *J. Phys. Chem. C* 119 (23) (2015) 13032–13040.

[47] H. Deng, J. Wang, Q. Peng, X. Wang, Y. Li, Controlled hydrothermal synthesis of bismuth oxyhalide nanobelts and nanotubes, *Chem. Eur. J.* 11 (2005) 6519–6524.

[48] C. Xiao, R. Liu, X. Hu, J. Zuo, L. Nan, L. Wang, Li, Oxygen-rich bismuth oxyhalides: generalized one-pot synthesis, band structures and visible-light photocatalytic properties, *J. Mater. Chem.* 22 (2012) 22840–22843.

[49] Y.R. Jiang, S.Y. Chou, J.L. Chang, S.T. Huang, H.P. Lin, C.C. Chen, Hydrothermal synthesis of bismuth oxybromide–bismuth oxyiodide composites with high visible light photocatalytic performance for the degradation of CV and phenol, *RSC Adv.* 5 (2015) 30851–30860.

[50] Y. Bai, T. Chen, P. Wang, L. Wang, L. Ye, Bismuth-rich $\text{Bi}_4\text{O}_5\text{X}_2$ ($X = \text{Br}$, and I) nanosheets with dominant {101} facets exposure for photocatalytic H_2 evolution, *Chem. Eng. J.* 304 (2016) 454–460.

[51] M. Thommes, K. Kaneko, A.V. Neimark, J.P. Olivier, F. Rodriguez-Reinoso, J. Rouquerol, K.S.W. Sing, Physisorption of gases, with special reference to the evaluation of surface area and pore size distribution (IUPAC Technical Report), *Pure Appl. Chem.* 87 (9–10) (2015) 1051–1069.

[52] J. Yu, J. Low, W. Xiao, P. Zhou, M. Jaroniec, Enhanced photocatalytic CO_2 -reduction activity of anatase TiO_2 by coexposed {001} and {101} facets, *J. Am. Chem. Soc.* 136 (25) (2014) 8839–8842.

[53] L. Ye, D. Wu, K.H. Chu, B. Wang, H. Xie, H.Y. Yip, P.K. Wong, Phosphorylation of $\text{g-C}_3\text{N}_4$ for enhanced photocatalytic CO_2 reduction, *Chem. Eng. J.* 304 (2016) 376–383.

[54] L. Ye, J. Liu, K. Deng, T. Peng, L. Zan, Facets coupling of $\text{BiOBr-g-C}_3\text{N}_4$ composite photocatalyst for enhanced visible-light-driven photocatalytic activity, *Appl. Catal. B: Environ.* 142–143 (2013) 1–7.

[55] L. Ye, J. Liu, C. Gong, L. Tian, T. Peng, L. Zan, Two different roles of metallic Ag on $\text{Ag}/\text{AgX/BiOX}$ ($X = \text{Cl}, \text{Br}$) visible light photocatalysts: surface plasmon resonance and Z-scheme bridge, *ACS Catal.* 2 (2012) 1677–1683.